Polar phonons and far-infrared amplitudon in $Sr_2Nb_2O_7$

2001 J. Phys.: Condens. Matter 13 2823

(http://iopscience.iop.org/0953-8984/13/12/307)

INSTITUTE OF PHYSICS PUBLISHING JOURNAL OF PHYSICS: CONDENSED MATTER

J. Phys.: Condens. Matter **13** (2001) 2823–2834 www.iop.org/Journals/cm PII: S0953-8984(01)21710-X

Polar phonons and far-infrared amplitudon in $Sr_2Nb_2O_7$

E Buixaderas, S Kamba and J Petzelt

Institute of Physics, ASCR, Na Slovance 2, 182 21 Prague 8, Czech Republic

E-mail: buixader@fzu.cz, kamba@fzu.cz and petzelt@fzu.cz

Received 7 February 2001

Abstract

Polarized far-infrared reflectivity and transmission measurements of an $Sr_2Nb_2O_7$ single crystal were performed in the temperature interval 10–550 K for the $\boldsymbol{E}\|\boldsymbol{a}$ and $\boldsymbol{E}\|\boldsymbol{c}$ polarizations. Modes at the centre of the Brillouin zone were analysed in the subsequent paraelectric–ferroelectric–incommensurate–monoclinic phases and the factor group analysis together with the correlation of the modes is presented. The ferroelectric A_1 soft mode revealed in Raman spectra below $T_c = 1613$ K was found in the $\boldsymbol{E}\|\boldsymbol{c}$ polarized infrared spectra. An amplitudon which softens to $T_i = 488$ K was observed in the incommensurate phase. On cooling the amplitudon anti-crosses a hard excitation near 33 cm^{-1} located in discommensurations and then, at about 100 K, also the ferroelectric soft mode. No evidence was found for the earlier suggested multiplication of the unit cell below the phase transition at $T_0 = 117$ K. Neglecting the small volume of discommensurations, we suggest the $Pb11$-C_S^2 space group ($Z = 4$) for the monoclinic phase below T_0.

1. Introduction

Strontium pyroniobate $Sr_2Nb_2O_7$ (SNO) is an interesting ferroelectric material for applications. The main advantages are its low coercive field and low permittivity, which enables it to be used in devices as a non-volatile ferroelectric memory based on field effect transistors (FETs) and capacitors (specially when doped with Ta) [1, 2], and optical waveguides [3]. SNO has one of the highest known ferroelectric phase transition temperatures, $T_c = 1615$ K [4], therefore it is very promising for high-temperature applications.

At room temperature the spontaneous polarization $P_s = 9 \times 10^{-2}$ C m^{-2} is parallel to the $\boldsymbol{c}$-axis and the coercive field is $E_c = 6 \times 10^3$ V cm^{-1} [4]. The SNO structure is a layered perovskite. It consists of a NbO_6 octahedra framework which distorts and tilts with temperature changes undergoing three phase transitions [5]. Above T_c (phase I) the symmetry group is assumed to be $Cmcm$-D_{2h}^{17} in analogy to the high-temperature paraelectric phase of $Sr_2Ta_2O_7$ [6] and below T_c (phase II) the established space group is $Cmc2_1$-C_{2v}^{12} [7] (see figure 1).

0953-8984/01/122823+12$30.00

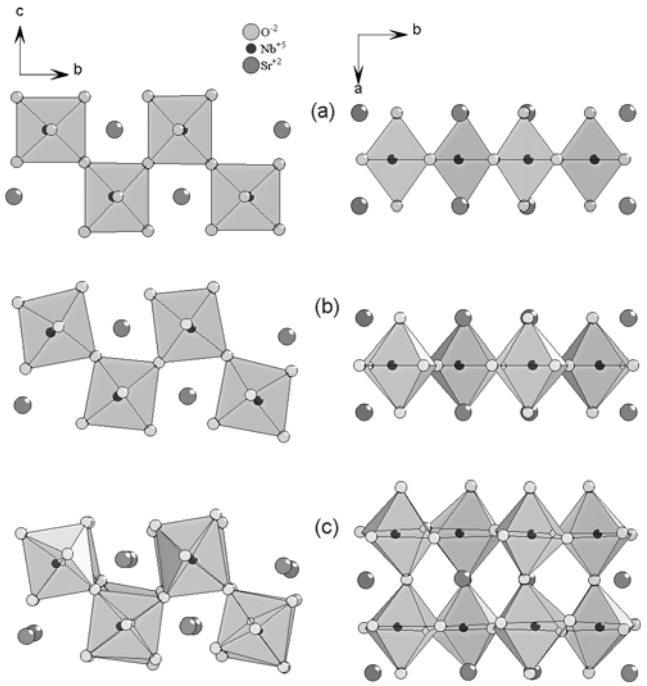

Figure 1. The primitive unit cell of SNO in the (a) paraelectric phase ($T > T_c = 1615$ K), (b) ferroelectric phase $T_c > T > T_i = 488$ K and (c) IC phase for $\delta = 0$ with the doubled volume ($T = 300$ K). The depicted volume corresponds to two primitive unit cells in (a) and (b), and to four in (c). O atoms are at the corners of the octahedra, Nb atoms are located inside each octahedron and Sr atoms are distributed among them.

At $T_i = 488$ K SNO undergoes a second-order phase transition to an incommensurate (IC) phase (phase III). This phase transition was revealed in the elastic compliance coefficients, electromechanical coupling and permittivity [8], and also by birefringence [9]. The modulation wave was observed in the [100] direction with the wave vector $\boldsymbol{q} = \pm(1/2\text{-}\delta)\boldsymbol{a}$, δ being temperature dependent [10]. The lock-in phase has not been found. δ decreases on cooling, first rapidly from 0.022 at 488 K to 0.01 at 300 K and then slowly ($\delta = 0.008$ at 55 K) without reaching zero value, therefore the crystal remains IC down to low temperatures. At room temperature, assuming $\delta = 0$, the space group reported is $Pbn2_1\text{-}C_{2v}^9$ [11] with the unit cell doubled along the $\boldsymbol{a}$-axis (see figure 1).

At $T_0 = 117$ K another phase transition (into a phase IV) takes place [12]. A pronounced dielectric anomaly was seen in $\varepsilon_b(T)$ and a new component of the spontaneous polarization appears along the $\boldsymbol{b}$-axis resulting in P_s lying in the bc-plane. The symmetry becomes monoclinic on average, with point group m [12]. It is interesting to note that no change in δ is seen when passing through T_0.

The dynamics of the phase transitions was studied mainly by means of Raman scattering. The ferroelectric soft mode was found in $b(cc)\bar{b}$ scattering configurations below T_c [13, 14]. Below T_i another soft mode appears confirming the displacive character of this phase transition. It seems to be coupled with another low-frequency mode because an intensity transfer between the two modes occurs [15, 16]. Raman [15] and ESR [17] experiments showed a non-classical behaviour of the IC order parameter with critical exponents $\beta = 0.38$ and $\beta = 0.34$ for the Raman soft mode frequency appearing below T_i and the amplitude of the IC wave modulation,

respectively. In the $a(bc)a$ and $b(ac)a$ Raman spectra the lowest modes partially soften towards T_0 and then harden [14, 18]. Also submillimetre $\boldsymbol{E}\|\boldsymbol{c}$ spectra [19] revealed another soft mode which hardens below T_0 from 13 to 18.5 cm^{-1}. It was suggested that it might be connected with a doubling of the unit cell at T_0.

No infrared (IR) measurements of SNO have been performed up to now, therefore the aim of this paper is to present IR reflectivity and far IR (FIR) transmission spectra, discuss the origin of the phase transitions from the lattice dynamical point of view, search for the amplitudon in the IC phase and discuss the symmetry below T_0 and the suggested doubling of the unit cell, comparing it with previous Raman and submillimetre spectra.

2. Experiment

An SNO single crystal was studied from 550 K down to 10 K by means of polarized IR reflectivity and FIR transmission spectroscopy. A polished colourless transparent b-plate (size $6.5 \times 8 \times 0.37$ mm^3) was used.

IR measurements were performed using the Fourier spectrometer Bruker IFS 113v equipped with room-temperature DTGS pyroelectric detectors as well as a He-cooled (1.5 K) Si bolometer. Spectra were obtained in the 15–2000 cm^{-1} range (below room temperature the range is limited to 15–650 cm^{-1} by the polyethylene windows used in the cryostat). For low-temperature measurements from 300 to 10 K a continuous-flow Oxford CF 104 cryostat, with the sample mounted on a cold finger in vacuum, was used for the reflection mode and for the transmission measurements an UTREX cryostat was used, where the sample is placed in a He gas bath. Measurements at high temperatures (300–550 K) were obtained using a home-made furnace. A thin metal mesh polyethylene polarizer was used to polarize the beam. The polarizer is opaque between 680 and 750 cm^{-1}, therefore the spectra are missing in this frequency region.

3. Results and evaluation

3.1. IR reflectivity and transmissivity measurements

The geometry of our sample enabled us to measure IR spectra only for the $\boldsymbol{E}\|\boldsymbol{a}$ and $\boldsymbol{E}\|\boldsymbol{c}$ polarizations. The temperature dependence of the reflectivity of the SNO single crystal is presented in figure 2 for both the polarizations. The spurious increase in the reflectivity at low temperatures below 50 cm^{-1} is due to the growing transparency of the sample. Low-temperature FIR $\boldsymbol{E}\|\boldsymbol{a}$ transmission spectra are shown, at selected temperatures, in figure 3. No interesting features were observed in $\boldsymbol{E}\|\boldsymbol{c}$ transmission spectra due to the low transparency at low temperatures. Experimental spectra were fitted with the factorized form of the generalized oscillator model of the complex dielectric function [20]

$$\hat{\varepsilon}(\omega) = \varepsilon'(\omega) - \mathrm{j}\varepsilon'' = \varepsilon_\infty \prod_{i=1}^{n} \frac{\omega_{LOi}^2 - \omega^2 + \mathrm{j}\omega\gamma_{LOi}}{\omega_{TOi}^2 - \omega^2 + \mathrm{j}\omega\gamma_{TOi}} \tag{1}$$

where ε_∞ is the permittivity at frequencies much higher than all oscillator eigenfrequencies, ω_{TOi} and ω_{LOi} are the eigenfrequencies of the transverse and longitudinal ith polar phonon mode respectively and γ_{TOi} and γ_{LOi} their respective damping constants. We took the values $\varepsilon_\infty^c = 4.62$ and $\varepsilon_\infty^a = 4.67$ from [9].

For the fit we have also used dielectric data at 1 MHz [4] and submillimetre spectra from [19] as well as our THz data measured at room temperature by time domain terahertz transmission spectroscopy [21], which gave us directly complex values of the dielectric function

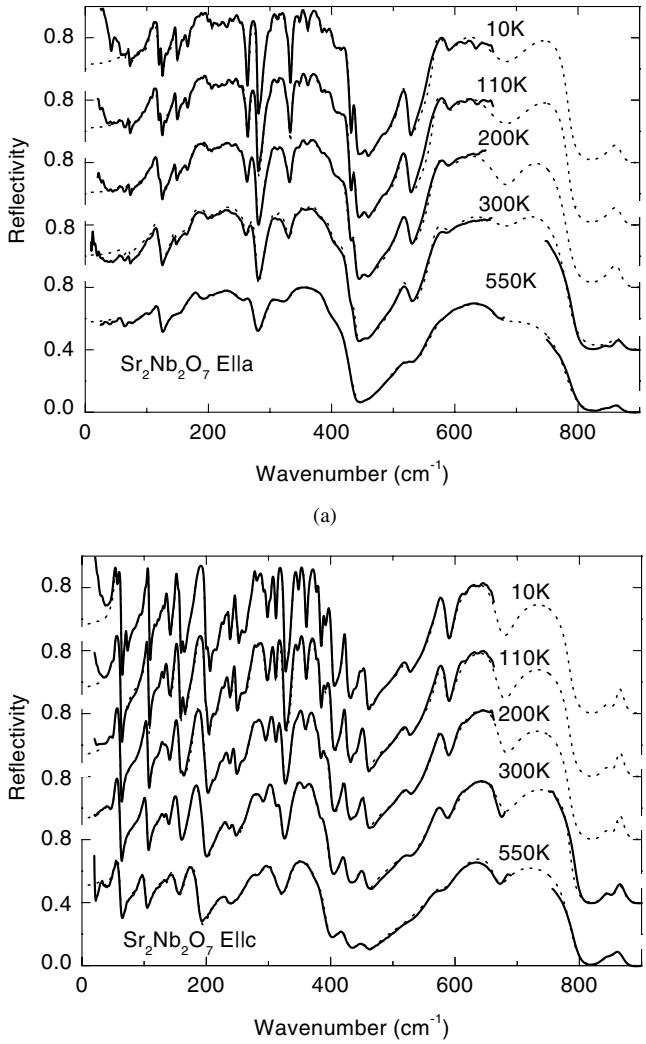

Figure 2. Temperature dependence of the reflectivity spectra of SNO for (a) $\boldsymbol{E}\|\boldsymbol{a}$ and (b) $\boldsymbol{E}\|\boldsymbol{c}$ polarizations. Solid curves correspond to the experiment and dotted curves to the fit. The spurious reflectivity increase in the experimental spectra below 50 cm^{-1} is caused by the growing transparency of the sample on cooling.

in the range 5–45 cm^{-1} (see figures 4 and 5). The permittivity $\varepsilon'(\omega)$ and loss spectra $\varepsilon''(\omega)$ calculated from our fits are shown, for selected temperatures, in figures 4 and 5, respectively, including the experimental THz points. The appearance of many new weak modes is seen on cooling due to the structural changes.

3.2. Factor-group analysis and symmetry considerations

We performed the factor-group analysis [22] of the parent phase of SNO using the structural data of the related compound $Sr_2Ta_2O_7$ [6], whose paraelectric phase *Cmmm* is isomorphous to that in SNO. This yields the phonon modes at the centre of the Brillouin zone (Γ-point) shown in table 1 for phase I. This analysis includes the three acoustic modes of symmetries

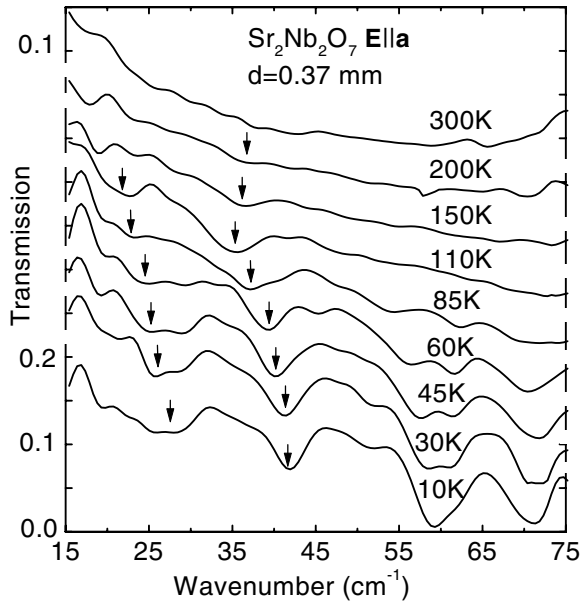

Figure 3. Temperature dependence of the FIR $\boldsymbol{E}\|\boldsymbol{a}$ polarized transmission spectra of SNO ($d = 0.37$ mm). The arrows show the positions of two temperature dependent modes.

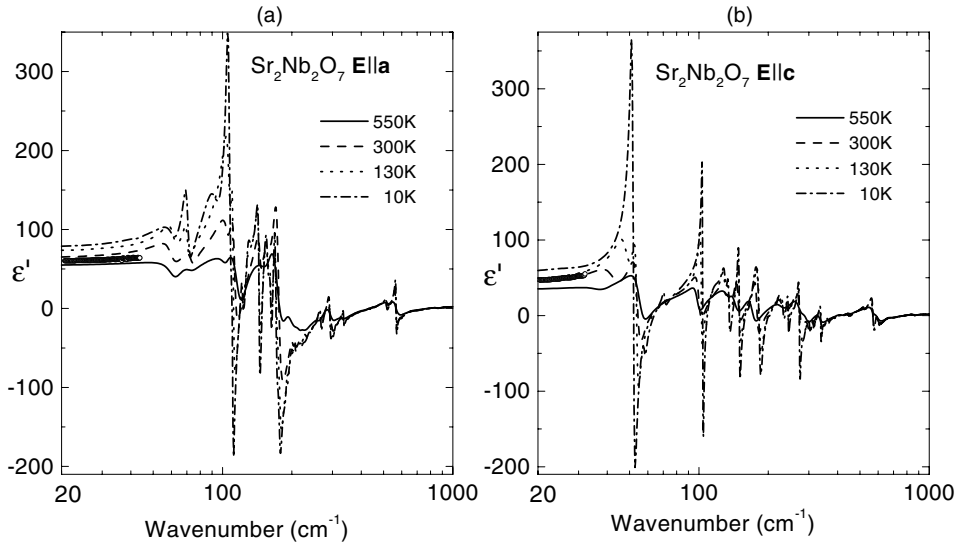

Figure 4. Temperature dependence of the permittivity $\varepsilon'(\omega)$ obtained from the fit in figure 1 with equation (1) for (a) $\boldsymbol{E}\|\boldsymbol{a}$ and (b) $\boldsymbol{E}\|\boldsymbol{c}$ polarizations. Points at 300 K correspond to the THz measurements. Note the logarithmic scale.

B_{1u}, B_{2u} and B_{3u}. The letters inside the parentheses denote the activities of the modes: a, b and c stand for $\boldsymbol{E}\|\boldsymbol{a}$, $\boldsymbol{E}\|\boldsymbol{b}$, and $\boldsymbol{E}\|\boldsymbol{c}$ polarized IR spectra, respectively, and doubled letters aa, ab etc for Raman activities in scattering geometries such as $a(ab)c$, where the first and second letter denotes the polarization of the incident and scattered waves, respectively. In total, we

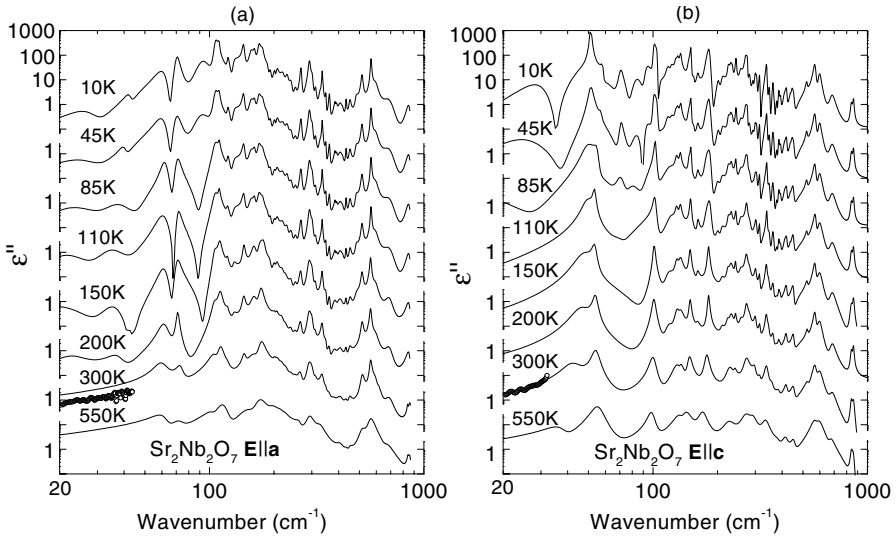

Figure 5. Temperature dependence of the loss spectra $\varepsilon''(\omega)$ obtained from the fit in figure 1 with equation (1) for (a) $\boldsymbol{E}\|\boldsymbol{a}$ and (b) $\boldsymbol{E}\|\boldsymbol{c}$ polarizations, showing the appearance of new modes. Points at 300 K correspond to the THz measurements. Note the logarithmic scales.

Table 1. Factor-group analysis of SNO in the different phases.

Phase I	Phase II	Phase III	Phase IV
$Cmmm$-D_{2h}^{17} $Z = 2$	$Cmc2_1$-C_{2v}^{12} $Z = 2$	$Pbn2_1$-C_{2v}^{9} $Z = 4$	$Pb11$-C_{s}^{2} $Z = 4$
	$\boldsymbol{B}_{1u} - m_{xz}m_{yz}2_z$ $P_s\|\|(001)$	$\boldsymbol{q} = \pm(1/2 - \delta)\boldsymbol{a}$ $(\delta = 0)$ $P_s\|\|(001)$	$\boldsymbol{B}_2 - m_x$ $(\delta = 0)$ $P_s \perp (100)$
10 $B_{1u}(c)$ 9 $Ag(aa, bb, cc)$	19 $A_1(c, aa, bb, cc)$	33 $A_1(c, aa, bb, cc)$	66 $A'(bc, aa, bb, cc, bc)$
11 $B_{2u}(b)$ 8 $B_{3g}(bc)$	19 $B_2(b, bc)$	33 $B_2(b, bc)$	
6 $A_u(-)$ 8 $B_{1g}(ab)$	14 $A_2(-, ab)$	33 $A_2(-, ab)$	66 $A''(a, ab, ac)$
9 $B_{3u}(a)$ 5 $B_{2g}(ac)$	14 $B_1(a, ac)$	33 $B_1(a, ac)$	
66 modes	66 modes	132 modes	132 modes

obtained 66 phonon modes, which follows from the two formula units in the primitive cell ($Z = 2$). The analysis by correlation into the ferroelectric phase gives the result shown in table 1 for phase II, where singlets A_1, B_1 and B_2 are the three acoustic modes. This can be obtained also using structural data by Ishizawa *et al* [7] with the atoms in the 4*a* and 4*b* Wickoff sites (see table 1). In our spectra we can see the A_1 and B_1 modes in the $\boldsymbol{E}\|\boldsymbol{c}$ and $\boldsymbol{E}\|\boldsymbol{a}$ polarized spectra, respectively. Our factor group analysis differs from that in [16], where it was erroneously assumed that all atoms are in 4*a* sites.

We performed also the factor group analysis of the hypothetical commensurate structure for $\delta = 0$ at room temperature, using the structural data by Scheunemann *et al* [11]. In total, 132 modes can be expected for phase III at the Γ-point (see table 1) due to the (approximate) doubling of the unit cell along the $\boldsymbol{a}$-axis below T_i ($Z = 4$). Factor group analysis using the

correlation into the monoclinic phase IV (point group m) below T_0—in the $\delta = 0$ case—is also shown in table 1. Note that both the above-mentioned analyses are simplified. The exact analysis for the IC phase ($\delta \neq 0$) allows the activation of many phonons from the whole Brillouin zone due to the folding at multiples of the incommensurate modulation vector. Only the zeroth-order processes are taken into account in our case, because the higher-order ones are expected to have a much lower spectral strength [23].

In table 1 the factor-group analysis for all the phases is summarized showing the correlation of the modes and the active representations responsible for the phase transitions. From the orthorhombic mmm point group, the B_{1u}-symmetry order parameter results in the orthorhombic $mm2$ point group with $\boldsymbol{P}_s \| \boldsymbol{c}$. From $mm2$, the B_2-symmetry order parameter results in the monoclinic m point group with a new component of the polarization $\boldsymbol{P}_s \| \boldsymbol{b}$. The possible space group for the monoclinic phase compatible with a ferroelectric phase transition being a subgroup of $Pbn2_1$ is $Pb11\text{-}C_S^2$.

In our room-temperature spectra we see 23 A_1 modes in the $\boldsymbol{E} \| \boldsymbol{c}$ and 30 B_1 modes in the $\boldsymbol{E} \| \boldsymbol{a}$ spectra, which is consistent with our simplified group analysis. The number of modes increases on cooling to 34 A_1 and 42 B_1 at 130 K, still in the orthorhombic IC phase, and then to 53 A' and 42 A'' at the lowest temperatures (10 K) in the monoclinic phase. The transverse frequencies of A_1 and B_1 modes (A' and A'', respectively, in the monoclinic phase) obtained from our IR fits are shown in table 2 at relevant temperatures: 550 K (above T_i), 300 K (below T_i), 130 K (just above T_0) and 10 K (the lowest temperature measured, in the monoclinic phase). The temperature evolution of the TO-mode frequencies below 100 cm^{-1} is shown in figure 6. The modes above 100 cm^{-1} do not show significant temperature dependence.

The number of observed IR modes in the IC phase is higher than predicted by the factor-group analysis (table 1). This can be explained by the approximation made in the analysis, which does not take into account new modes which may activate due to the folding at multiples of the IC modulation vector. The number of IR modes in the lowest phase is consistent with that theoretically predicted by the change to monoclinic symmetry without multiplication of the unit cell.

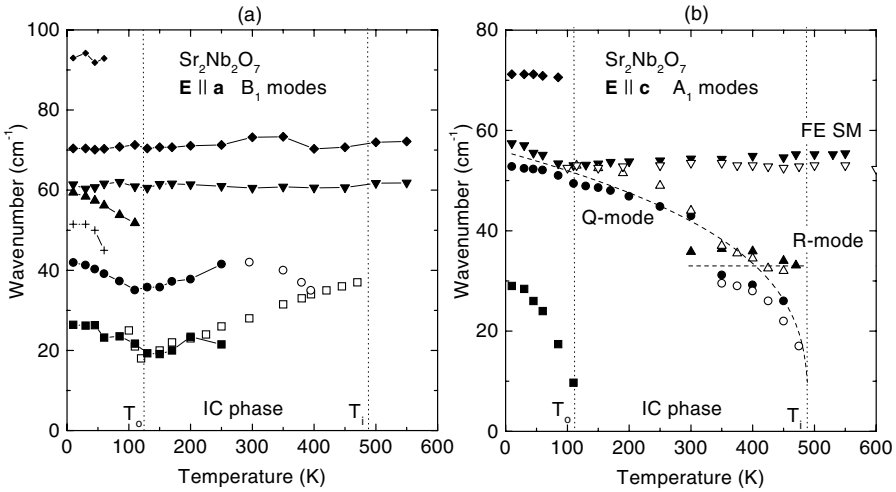

Figure 6. Temperature dependence of IR active TO-mode frequencies of an SNO single crystal below 100 cm^{-1} for (a) $\boldsymbol{E} \| \boldsymbol{a}$ and (b) $\boldsymbol{E} \| \boldsymbol{c}$ polarizations, obtained from the fit. Open symbols denote Raman modes from [13–17]. The dashed curve denotes the fit $\omega_Q = A(T_i - T)^{\beta}$ with $T_i = 488$ K, $A = 8.68 \pm 0.05$ cm^{-1} $K^{-\beta}$ and $\beta = 0.3 \pm 0.03$.

Table 2. Frequencies of the IR active TO modes (in cm^{-1}) at several temperatures for the $\boldsymbol{E}\|\boldsymbol{a}$ and $\boldsymbol{E}\|\boldsymbol{c}$ polarizations.

$\boldsymbol{E}\|\boldsymbol{c}$ A_1/A' modes				$\boldsymbol{E}\|\boldsymbol{a}$ B_1/A'' modes			
550 K	300 K	130 K	10 K	550 K	300 K	130 K	10 K
—	—	—	30.1	—	—	19.3	28.0
37.6	42.3	48.9	47.4	—	—	35.8	42.5
55.4	54.1	53.1	51.2				
—	—	—	58.3	61.8	60.5	60.5	61.4
—	—	—	70.6	72.2	73.2	70.4	70.4
—	—	—	82.7	—	—	—	93.0
—	—	—	92.8				
—	—	—	100.9				
98.7	100.1	102.3	104.4	103.7	105.0	107.3	106.7
—	—	118.7	117.2	117.2	113.3	110.7	110.7
—	—	—	121.4	—	121.2	121.2	121.8
—	—	—	127.4	—	—	127.8	128.7
—	130.8	129.1	130.1				
134.2	134.4	134.0	134.6				
—	—	—	146.1	—	145.5	144.7	144.4
142.5	147.7	149.7	150.3	—	—	156.5	156.7
—	—	—	155.5	157.1	161.6	162.2	162.2
—	—	161.1	162.0	170.8	174.0	170.2	170.2
170.4	178.1	179.0	176.6	—	—	176.8	176.8
—	—	184.2	183.0	—	—	—	187.6
—	—	—	201.6	—	—	192.2	192.2
—	—	209.5	209.6	194.5	202.2	201.6	202.1
227.1	228.0	224.2	224.3	—	205.5	205.5	205.8
—	—	230.9	230.5	217.2	221.0	220.0	220.6
—	—	—	234.7	220.5	224.3	229.4	230.8
—	240.3	242.8	243.9	241.6	240.1	240.7	240.8
—	—	255.2	255.8	—	251.7	252.3	252.3
271.5	272.7	273.2	270.2	261.6	265.6	266.9	267.3
—	—	—	275.8				
—	—	282.6	282.4				
—	—	—	293.7	293.0	291.4	292.5	292.6
—	—	—	300.3	—	301.3	301.3	301.4
292.6	298.0	302.4	304.2				
—	315.4	314.3	314.2	311.5	311.4	311.7	311.9
—	—	—	331.4	—	—	328.1	328.2
335.1	338.2	339.4	338.6	326.8	335.5	335.4	335.4
—	—	348.5	348.9	—	349.4	349.5	349.4
—	—	—	362.8	—	362.4	362.9	362.8
—	358.5	363.0	369.0				
—	—	379.8	378.7	382.4	385.5	386.3	386.2
384.2	387.3	386.6	386.8	—	—	390.8	390.8
—	—	393.3	393.7	404.9	409.7	408.4	409.2
—	—	—	410.5	—	—	416.8	416.8
416.3	418.2	419.6	419.9	433.6	434.2	432.7	433.7
—	—	436.9	437.6	449.8	451.1	451.2	452.3
—	—	—	446.9	—	—	482.6	482.2
453.3	452.8	451.3	451.5	516.8	515.8	514.0	514.6
—	527.3	521.8	521.2	564.2	564.2	566.9	566.9
571.9	569.4	571.6	569.1	599.3	592.2	593.7	593.7
590.8	597.0	597.0	597.3	604.8	604.8	604.8	604.8
671.9	683.4	683.4	683.4	664.2	664.2	664.2	664.2
842.8	842.1	842.1	842.1	844.2	844.2	844.2	844.2
858.3	860.6	860.6	860.6	861.1	861.1	861.1	861.1

4. Discussion

In the $\boldsymbol{E}\|\boldsymbol{a}$ polarization several new modes are seen in the transmission spectra below 100 cm^{-1} (see figures 3 and 6(a)). Some new modes appear also in the IR reflectivity spectra below T_0. B_1 modes become of A″ symmetry due to the phase transition into the monoclinic phase (see table 1). Partial softening of the B_1 modes near 40 and 25 cm^{-1} is seen. No quantitative understanding of this softening is so far available.

In the $\boldsymbol{E}\|\boldsymbol{c}$ polarized spectra two A_1 modes with anomalous temperature behaviour are seen (see figure 6(b)). The one near 55 cm^{-1} is almost temperature independent in our spectra down to T_0 and then its frequency rises. This mode was seen in Raman scattering [13, 14] showing pronounced softening towards T_c and was assigned to the ferroelectric soft mode. The second anomalous mode ($\omega \sim 35$ cm^{-1} near T_i) appears below T_i only and corresponds also to another mode observed in Raman spectra [14]. These two soft modes are probably connected with NbO_6 octahedra tiltings. Below T_c the ordered octahedra rotate within the layers, in the *bc* plane (see figure 1(b)). The eigen-vector of the ferroelectric soft mode may be connected with these tiltings and the magnitude of the tilt might be the order parameter of the ferroelectric phase transition, as commonly occurs in perovskites. At T_i the octahedra tilt in different ways in adjacent layers resulting in the IC modulation. For $\delta = 0$ (in the hypothetical lock-in phase) this produces a doubling of the unit cell along the $\boldsymbol{a}$-axis [24] (see figure 1(c)) because the tiltings in the adjacent layers are in anti-phase. The eigen-vector of the amplitudon might be related mainly to these anti-tiltings, although as secondary effect the octahedra are deformed so that the planes inside the octahedra are not coplanar with the *bc* layers of the crystal.

An unusual effect is the appearance of a Raman mode around 27 cm^{-1} below T_i which interacts with the other newly activated mode near 35 cm^{-1} and then disappears at 300 K (see figure 6(b) and [15]). Although A_1 modes are simultaneously Raman and IR active, we could not see directly this mode in our IR spectra because the sample is not transparent at high temperatures and reflectivity is not sensitive enough for observation of weak modes. Therefore, we used previous dielectric loss spectra from submillimetre measurements [19] (in which the softening of a mode of higher frequency than 20 cm^{-1} is indirectly indicated) together with our IR data during the fitting process below T_i. With this procedure we succeeded in evaluating the frequencies of the two modes below T_i which are in agreement with those from Raman measurements (see figure 6(b)) and have to be connected with the normal ferroelectric–incommensurate phase transition. Above T_i our IR spectra are not accurate enough below 50 cm^{-1} to allow us to draw definite conclusions about the modes in this region.

Looking more in detail at the interaction of the new modes below T_i and by comparison with Raman data [15], we see that the modes seem to undergo an anti-crossing as shown in figure 6(b) by the broken lines. This means that there is a mode which appears below T_i following the line corresponding to a power law $\omega = A(T_i - T)^{\beta}$ with $T_i = 488$ K, $A = 8.68 \pm 0.05$ cm^{-1} $K^{-\beta}$ and $\beta = 0.3 \pm 0.03$ (it will be called the Q-mode). On its way it anti-crosses a mode of constant frequency near 33 cm^{-1} (we denote it as the R-mode) and their coupling causes a repulsion between the two modes resulting in the coupled-mode frequencies observed. The index $\beta = 0.3 \pm 0.03$ of the temperature behaviour of the Q-mode frequency does not follow the classical behaviour, but it is in agreement with the reported values $\beta = 0.34 \pm 0.02$ for the amplitude of the IC wave modulation [17] and $\beta = 0.38 \pm 0.02$ for the frequency of the Raman soft mode appearing below T_i [15]. However, we do not believe that this feature manifests unambiguously a non-classical behaviour for the order parameter of the IC phase, because such a behaviour might be expected in a narrow temperature range below T_i only. It might be rather caused by higher-order terms in the Landau-type free energy expansion.

On further cooling the Q-mode interacts with the ferroelectric soft mode at about 55 cm^{-1} near 100 K and undergoes a repulsion which can be seen in figure 6(b). Both their frequencies and intensities anti-cross near 100 K, indicating an interaction. The modes also exchange their oscillator strength ($f = \Delta\varepsilon\,\omega^2$), the Q-mode becoming weaker and the ferroelectric soft mode stronger below 100 K. It can be seen that the temperature behaviour of the Q-mode frequency follows the broken line in figure 6(b) in a more natural way, which corresponds to its fit. This mode is the full-symmetry soft mode which may become IR active below T_i for a polar symmetry and, therefore, it represents the amplitudon (amplitude fluctuations of the complex order parameter) for the IC phase transition [23], contributing also to the small anomaly seen in ε_c at T_i.

The behaviour of the two soft A_1 modes below T_i (the ferroelectric one and the amplitudon–Q-mode) has been the subject of Raman investigations concerning their coupling near T_0 [16]. We tried also to study this effect in our IR spectra using a two-coupled-oscillator model. In this case the complete dielectric function is treated as a sum of n damped oscillators, two of them being coupled through a real constant α which renormalizes their eigen-frequencies [25]:

$$\hat{\varepsilon}(\omega) = \frac{\Delta\varepsilon_1\omega_1^2(\omega_2^2 - \omega^2 + \mathrm{j}\omega\gamma_2) + \Delta\varepsilon_2\omega_2^2(\omega_1^2 - \omega^2 + \mathrm{j}\omega\gamma_1) - 2(\Delta\varepsilon_1\Delta\varepsilon_2)^{1/2}\omega_1\omega_2\alpha}{(\omega_1^2 - \omega^2 + \mathrm{j}\omega\gamma_1)(\omega_2^2 - \omega^2 + \mathrm{j}\omega\gamma_2) - \alpha^2} + \sum_{i=3}^{n} \frac{\Delta\varepsilon_i\omega_i^2}{(\omega_i^2 - \omega^2 + j\omega\gamma_i)} + \varepsilon_\infty. \tag{2}$$

We were able to reproduce the spectra using temperature-independent coupling ($\alpha = -330$ cm^{-2}) and found that the bare frequencies of the ferroelectric soft mode and the Q-mode cross near 100 K as shown in figure 7. The observed interchange of the oscillator strengths ($f_i = \Delta\varepsilon_i\,\omega_i^2$) of the coupled modes proves the crossing feature of the bare mode frequencies. After decoupling the modes, their oscillator strengths behave in a normal way without pronounced temperature dependences (figure 7 inset).

Regarding the IC structure, just below T_i the modulation wave is expected to be sinusoidal. On cooling, the decrease in δ and the appearance of higher harmonics in the modulation usually deform the modulation wave to a picture of a domain-like pattern (soliton picture) in which the IC regions (discommensurations) become reduced to periodic domain walls between quasi-commensurate domains [23]. In the case of SNO, when δ is very small, the domain pattern may appear and the volume fraction of IC regions in the whole crystal is small with respect to the commensurate ones. Therefore the crystal structure can be considered almost as a commensurate one. This is a factor which might explain the behaviour of the Q- and R-mode strengths. The R-mode, which is seen below T_i, disappears near 300 K probably because it is a mode localized only in the discommensurations. Below about 300 K this volume becomes very small and the intensity of the R-mode on average becomes very weak and almost negligible. The Q-mode is the amplitudon which appears below T_i and remains active also in the commensurate phase [23]. At T_0 the commensurate part of the crystal undergoes the phase transition to the monoclinic phase. This hypothesis is in agreement with [17], where the soliton picture is applied to describe the crystal structure below 393 K.

Below T_0 we do not see the soft mode which was observed in submillimetre spectra near 15 cm^{-1} for $\boldsymbol{E}\|\boldsymbol{c}$ [19], because its frequency lies below the limit of our spectral range. Nevertheless, its temperature dependence is reproduced in figure 6(b). The phase transition at T_0 is connected with a dielectric anomaly in $\varepsilon_b(T)$ [12]. This means that the new soft mode above T_0 should be of B_2 symmetry, active in the $\boldsymbol{E}\|\boldsymbol{b}$ spectra (see table 1). This spectrum could not be measured in our case. Below T_0, the appearance of another component of the polarization along the $\boldsymbol{b}$-axis causes $\boldsymbol{P}_s$ to rotate from the $\boldsymbol{c}$-direction and to lie generally in

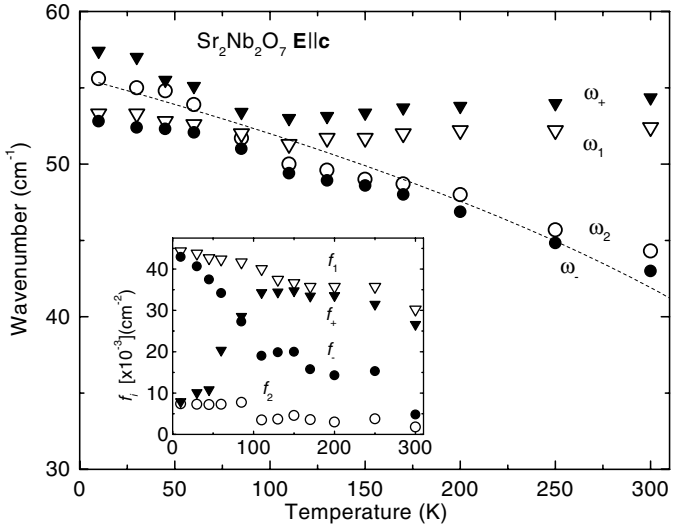

Figure 7. Temperature dependences of the bare and coupled mode frequencies of the ferroelectric soft mode (ω_1 and ω_+, respectively) and the amplitudon Q-mode (ω_2 and ω_-, respectively). The corresponding oscillator strengths $f_i = \Delta\varepsilon_i\,\omega_i^2$ are in the inset. Bare modes (ω_1, ω_2 in equation (2)) are marked by open symbols. Full symbols denotes the coupled modes (ω_+, ω_-) using the fit with equation (1).

the *bc*-plane. Therefore, the strong soft mode in the $\boldsymbol{E}\|\boldsymbol{b}$ polarization becomes weakly active also in the $\boldsymbol{E}\|\boldsymbol{c}$ spectra. Active modes in the $\boldsymbol{E}\|\boldsymbol{b}$ and $\boldsymbol{E}\|\boldsymbol{c}$ spectra become of the same A′ symmetry as seen from our group analysis (table 1). This explains the weak strength of this mode in the $\boldsymbol{E}\|\boldsymbol{c}$ submillimetre spectra [19].

The contributions of B_1 IR modes to the permittivity account for the values measured below 550 K in the submillimetre region, $\varepsilon'_a \sim 60$–70. Below submillimetre frequencies another dispersion has to take place to give the values $\varepsilon'_a \sim 90$–100 measured at MHz and kHz frequencies [4, 8, 12]. The discrepancy between submillimetre and MHz values of ε'_a decreases on cooling but is present down to 10 K. Its origin could be connected with the structural disorder due to the remaining discommensurations.

In the $\boldsymbol{E}\|\boldsymbol{c}$ spectra there is a small difference between the submillimetre value of ε'_c above 300 K and our estimations from the IR fit. This indicates that between IR and submillimetre frequencies there is some dispersion (probably also caused by the lattice disorder) which should account for the difference $\varepsilon_{SMM} - \varepsilon_{ph} \sim 20$. Below 300 K this difference tends to vanish and no dispersion is observed down to the kHz range at 10 K.

5. Conclusions

Previous Raman measurements [13] revealed a soft mode of A_1 symmetry which drives the high-temperature ferroelectric phase transition in SNO. This mode was also seen in our FIR $\boldsymbol{E}\|\boldsymbol{c}$ spectra, although its temperature dependence very far below T_c is extremely weak. In the IC phase, below $T_i = 488$ K, two new modes of frequencies near 35 cm^{-1} and 20 cm^{-1} appear. These modes are the result of a coupling of a hard mode of constant frequency (near 33 cm^{-1}) and a new soft mode—an amplitudon—appearing below T_i. The hard mode is assumed to be localized in the IC regions of the crystal, which explains its disappearance in the quasi-commensurate domain-like regime dominating below 300 K. On further cooling the

amplitudon interacts with the ferroelectric soft mode and near 100 K both modes exchange their oscillator strengths.

The hypothesis of a new doubling of the unit cell at $T_0 = 117$ K [19] is not confirmed. All the new modes in IR spectra are satisfactory explained by the equitranslational symmetry change from the orthorhombic to the monoclinic structure. A_1 and B_2 modes transform into A' modes showing the same activity, which is the reason for detecting the soft mode in the $\boldsymbol{E}\|\boldsymbol{c}$ spectra.

Acknowledgments

The authors would like to thank P Kuzel for the help with the time resolved THz measurements. The work was supported by the Grant Agency of the Czech Republic (projects Nos 202/98/1282, 202/01/0612), the Grant Agency of the Academy of Sciences of the Czech Republic (project No A1010828) and the Basque Government (PhD scholarship of the programme 'Formación de investigadores del Departamento de Educación, Universidades e Investigación').

References

[1] Fujimori Y, Nakamura T and Kamisawa A 1998 *Japan. J. Appl. Phys.* **37** 5207
[2] Fujimori Y, Nakamura T and Kamisawa A 1999 *Japan. J. Appl. Phys.* **38** 2285
[3] Ishitani A and Kimura M 1976 *Appl. Phys. Lett.* **29** 289
[4] Nanamatsu S, Kimura M and Kawamura T 1975 *J. Phys. Soc. Japan* **38** 817
[5] Isupov V A 1999 *Ferroelectrics* **220** 79
[6] Ishizawa N, Maruno F, Kawamura T and Kimura M 1976 *Acta Crystallogr.* B **32** 2 564
[7] Ishizawa N, Maruno F, Kawamura T and Kimura M 1975 *Acta Crystallogr.* B **31** 1912
[8] Ohi K, Kimura M, Ishida H and Kakinuma H 1979 *J. Phys. Soc. Japan Lett.* **46** 1387
[9] Akishige Y, Yoneya Y, Ohi K and Sawaguchi E 1989 *J. Phys. Soc. Japan Lett.* **58** 398
[10] Yamamoto N, Yagi K, Honjo G, Kimura M and Kawamura T 1980 *J. Phys. Soc. Japan* **48** 185
[11] Scheunemann K and Muller-Buschbaum H K 1975 *J. Inorg. Nucl. Chem.* **37** 1679
[12] Akishige Y, Kobayashi M, Ohi K and Sawagachi E 1986 *J. Phys. Soc. Japan* **55** 2270
[13] Kojima S, Jang M, Ohi K and Nakamura T 1981 *J. Phys. Soc. Japan Lett.* **50** 2787
[14] Ohi K and Kojima S 1985 *Japan. J. Appl. Phys.* **24** (Suppl 2) 817
[15] Kojima S, Ohi K, Takashige M, Nakamura T and Kakinuma H 1979 *Solid State Commun.* **31** 755
[16] Ito K, Horokoshi T and Ohi K 1997 *Ferroelectrics* **203** 201
[17] Akisige Y, Kubota T and Ohi K 1983 *J. Phys. Soc. Japan* **52** 1290
[18] Ohi K, Omura H, Kazumi T, Takasigue M, Jang M and Nakamura T 1982 *J. Phys. Soc. Japan* **51** 3745
[19] Volkov A A, Ishibashi Y, Kozlov G V, Lebedev S P, Petzelt J and Prokhorov A M 1980 *J. Phys. Soc. Japan* **49** (Suppl B) 78
[20] Kurosawa T 1961 *J. Phys. Soc. Japan* **16** 1298
[21] Kuzel P and Petzelt J 2000 *Ferroelectrics* **239** 79
[22] Rousseau D L. Baumann R P and Porto S P S 1981 *J. Raman Spectrosc.* **10** 253
[23] Petzelt J 1981 *Phase Transitions* **2** 155
[24] Yamamoto N 1982 *Acta Crystallogr* A **38** 780
[25] Petzelt J, Kozlov G V and Volkov V V 1987 *Ferroelectrics* **73** 101